DETACHED-EDDY SIMULATION OF THE SEPARATED FLOW AROUND A FOREBODY CROSS-SECTION

Kyle D. Squires[1], James R. Forsythe[2] and Philippe R. Spalart[3]

[1] *Mechanical and Aerospace Engineering Department, Arizona State University, Tempe, AZ 85287-6106, USA*
squires@asu.edu

[2] *Department of Aeronautics, United Air Force Academy, Colorado Springs, CO 80840-6222, USA*
jim.forsythe@usafa.af.mil

[3] *Boeing Commercial Airplanes, Seattle, WA 98124-2207, USA*
philippe.r.spalart@boeing.com

Abstract

Detached-Eddy Simulation (DES) is used to predict the massively separated flow around a forebody cross section. The configuration is the flow at 10° angle of attack over a rounded-corner square. The spanwise coordinate of the flow is statistically homogeneous with periodic end conditions employed in the calculations. Simulations are performed at sub- and super-critical Reynolds numbers for which experimental measurements show a reversal of the lateral (side) force acting on the body. DES predictions are evaluated using experimental measurements and unsteady Reynolds-averaged Navier-Stokes (URANS) results for a modest range of grid refinement, in calculations with a doubling of the spanwise period, and using simulations performed without an explicit turbulence model.

Sub- and super-critical flows are computed at Reynolds numbers of 10^5 and 8×10^5, respectively. Boundary layer separation characteristics (laminar or turbulent) are established via the initial and boundary conditions of the calculations. Following flow detachment, a chaotic and three-dimensional wake rapidly develops. For the super-critical flow, the pressure distribution is close to the measured values and both the streamwise and lateral forces are in adequate agreement with measurements. For the sub-critical flow, DES predictions are sufficiently far from the experimental measurements that side-force reversal is not predicted. Possible causes for the discrepancy are discussed.

Keywords:

Turbulence simulation and modeling, high Reynolds number prediction

1. Introduction

Knowledge of the spin and recovery characteristics of modern aircraft is crucial at a variety of levels, including maneuverability, control strategies, and ultimately design. One of the most significant factors affecting spin characteristics is the forebody, with its complex vortical flows and long moment arm. Laboratory measurements of spin characteristics are of limited utility since it is not possible to resolve important Reynolds number effects because of the range of available tunnels. Numerical simulation, therefore, provides an important tool that should ultimately provide higher-fidelity evaluations of aircraft spin than current approaches.

Unfortunately, numerical models are not adequate in many instances due to their inability to accurately predict the complex and unsteady effects associated with spin. Vortical flows, crossflow separations, and sensitivity of forces and moments to Reynolds number significantly challenge modeling approaches. These factors also supply the overall motivation for the present investigations and the need to develop and assess improved techniques for predicting complex, separated flows at high Reynolds numbers.

Most high-Reynolds number predictions are currently obtained from solutions of the Reynolds-averaged Navier-Stokes (RANS) equations. While the most popular RANS models appear to yield predictions of comparable accuracy in attached flows as well as those with shallow separations, RANS predictions of massive separations have typically been unreliable. RANS models, calibrated in thin shear layers, appear unable to consistently represent to sufficient accuracy the chaotic and unsteady features of massively separated flows.

The relatively poor performance of RANS models has motivated the increased application of Large Eddy Simulation (LES). Away from solid surfaces, LES is a powerful approach, providing a description of the large, energy-containing scales of motion that are typically dependent on geometry and boundary conditions. When applied to boundary layers, however, the computational cost of whole-domain LES does not differ significantly from that of Direct Numerical Simulation (DNS) (Chapman 1979, Spalart *et al.* 1997). The "large eddies" close to the wall are physically small in scale and in high Reynolds number boundary layers, LES may not sufficiently resolve near-wall structures, leading to inaccurate descriptions of boundary layer growth and/or separation.

In the present contribution, predictions are obtained using Detached-Eddy Simulation (DES), a hybrid method which has RANS behavior near the wall and becomes a Large Eddy Simulation in the regions away from solid surfaces where the grid density is sufficient (Spalart *et al.* 1997). The formulation used here is based on a modification to the Spalart-Allmaras one-equation model (Spalart and Allmaras 1994, referred to as S-A throughout) and is described in greater detail in the next section. DES is a non-zonal technique that is computationally feasible for high Reynolds number prediction, but also resolves time-dependent, three-dimensional turbulent motions as in LES. Previous applications of the method have been favorable, yielding adequate predictions across a range of flows and also showing the computational cost exhibits a weak dependence on Reynolds number, similar to RANS methods yet at the same time providing more realistic descriptions of unsteady effects (see Strelets 2001 for a recent review).

The study described in this manuscript is a pre-cursor to the ultimate application which is prediction of the spin characteristics of full aircraft at flight Reynolds numbers. Progress in modeling a full aircraft using DES is reported by Squires *et al.* (2001). The flow fields characterizing spinning aircraft are massively separated, providing a "natural" application for DES. Though a natural application for the model, calculations of complex configurations at high Reynolds numbers challenge the entire computational approach, especially the process of grid generation. Given the end application, unstructured grids form an integral component of the present approach and an unstructured-grid solver is employed for numerical solution of the Navier-Stokes equations. The disadvantage of the current unstructured approach is that the numerical procedure is second-order accurate in time and space and stabilized via non-linear (TVD) numerical dissipation. Related investigations have shown that the artificial dissipation associated with the numerical scheme can be as large as that represented by the turbulence model and therefore care must be exercised in application of these methods to eddy-resolving simulations such as LES (e.g., see Mittal and Moin 1999). This in turn motivates another goal of the work – to explore the accuracy of the current second-order method on both structured and unstructured grids for DES applications.

The flow considered is that around a canonical forebody cross section, the rounded-corner square shown in Figure 1. The corner radius is 1/4 of the width/height ("diameter", D) of the forebody, similar to the cross-sections of the X-29 and T-38. Numerical predictions are compared to the experimental measurements from Polhamus *et al.* (1959). These investigators measured the forces on a variety of forebody cross-sections over a range of Reynolds numbers and angles of attack. For the rounded-corner square, pressure coefficients around the forebody were also reported.

For the simulations reported in this manuscript, the angle of attack, α, of the freestream velocity is $10°$. In the sub-critical regime (Reynolds numbers below about 5×10^5), boundary layer separation along the top surface (upper-most horizontal surface in Figure 1) occurs near the upper-front corner of the forebody, while for the super-critical flows the boundary layer remains attached along the upper surface. The changes in boundary layer separation characteristics have significant effects on the streamwise and lateral forces with Reynolds number (the lateral, or side, force acts along the y axis in Figure 1). A re-

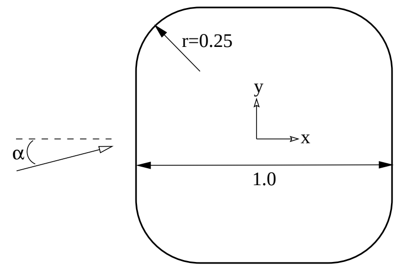

Figure 1. Flow configuration. Corner radius is 1/4 the "diameter" D of the forebody. Angles are measured positive counterclockwise from the aft-symmetry stagnation point.

versal of the lateral force was measured in the experiments, i.e., negative for sub-critical flows and positive in the super-critical regime. Relevant to spin, the negative side force in the sub-critical regime is spin-propelling, while at the higher Reynolds numbers the positive side force is spin-damping.

The main objectives of the work have been to both understand forebody spin characteristics as it relates to side-force reversal and to assess/advance DES as a viable method for prediction of unsteady flows at high Reynolds numbers. The stability of DES results with changes in grid refinement is investigated, as well as other factors such as the dimension of the (statistically homogeneous) spanwise coordinate. DES results are also compared to predictions obtained from the unsteady Reynolds-averaged Navier-Stokes (URANS) equations (of both the two- and three-dimensional equations) and to simulations performed without an explicit turbulence model. The runs without a turbulence model are denoted as MILES (Monotone Integrated Large Eddy Simulation) to provide a link with relevant literature, although no detailed investigations were undertaken to evaluate the numerical dissipation in the current calculations and its role as an SGS model, and the numerical schemes are not monotone in a strict sense (see Fureby and Grinstein 1999 for further discussion of the MILES approach).

2. Computational Approach

2.1 Detached-Eddy Simulation

The DES formulation in this study is based on a modification to the S-A model such that it reduces to RANS close to solid surfaces and to LES away from the wall (Spalart *et al.* 1997). The S-A RANS model is written as (see Spalart and Allmaras 1994),

$$\frac{D\widetilde{\nu}}{Dt} = c_{b1}[1-f_{t2}]\widetilde{S}\,\widetilde{\nu} + \frac{1}{\sigma}\left[\nabla\cdot((\nu+\widetilde{\nu})\nabla\widetilde{\nu}) + c_{b2}\,(\nabla\widetilde{\nu})^2\right]$$

$$- \quad \left[c_{w1} f_w - \frac{c_{b1}}{\kappa^2} f_{t2}\right] \left[\frac{\tilde{\nu}}{d}\right]^2 + f_{t1}\, \Delta U^2 \,, \tag{1}$$

where $\tilde{\nu}$ is the working variable. The eddy viscosity ν_t is obtained from,

$$\nu_t = \tilde{\nu}\, f_{v1}, \qquad f_{v1} = \frac{\chi^3}{\chi^3 + c_{v1}^3}, \qquad \chi \equiv \frac{\tilde{\nu}}{\nu} \,, \tag{2}$$

where ν is the molecular viscosity. The production term is expressed as,

$$\tilde{S} \equiv f_{v3} S + \frac{\tilde{\nu}}{\kappa^2 d^2} f_{v2} \,, \tag{3}$$

$$f_{v2} = \left(1 + \frac{\chi}{c_{v2}}\right)^{-3}, \qquad f_{v3} = \frac{(1 + \chi f_{v1})(1 - f_{v2})}{\chi} \,, \tag{4}$$

where S is the magnitude of the vorticity. The production term as written in (3) differs from that developed in Spalart and Allmaras (1994) via the introduction of f_{v3} and re-definition of f_{v2}. These changes do not alter predictions of fully turbulent flows and have the advantage that for simulation of flows with laminar separation, numerical diffusion upstream of the eddy viscosity into attached, laminar regions is prevented. The function f_w is given by,

$$f_w = g\left[\frac{1 + c_{w3}^6}{g^6 + c_{w3}^6}\right]^{1/6}, \qquad g = r + c_{w2}\,(r^6 - r), \qquad r \equiv \frac{\tilde{\nu}}{\tilde{S}\kappa^2 d^2} \,. \tag{5}$$

The function f_{t2} is defined as,

$$f_{t2} = c_{t3} \exp(-c_{t4}\chi^2) \,. \tag{6}$$

The trip function f_{t1} is specified in terms of the distance d_t from the field point to the trip, the wall vorticity ω_t at the trip, and ΔU which is the difference between the velocity at the field point and that at the trip,

$$f_{t1} = c_{t1} g_t \exp\left(-c_{t2} \frac{\omega_t^2}{\Delta U^2}\left[d^2 + g_t^2 d_t^2\right]\right) \,, \tag{7}$$

where $g_t = \min(0.1, \Delta U / \omega_t \Delta x)$ where Δx is the grid spacing along the wall at the trip. For the current simulations, f_{t1} was set to zero to alleviate the high cost of evaluating d_t in an unstructured code. For simulations in which the flow is tripped, large levels of eddy viscosity are added at designated trip locations. The wall boundary condition is $\tilde{\nu} = 0$. The constants are $c_{b1} = 0.1355$, $\sigma = 2/3$, $c_{b2} = 0.622$, $\kappa = 0.41$, $c_{w1} = c_{b1}/\kappa^2 + (1 + c_{b2})/\sigma$, $c_{w2} = 0.3$, $c_{w3} = 2$, $c_{v1} = 7.1$, $c_{v2} = 5$, $c_{t1} = 1$, $c_{t2} = 2$, $c_{t3} = 1.1$, and $c_{t4} = 2$.

The DES formulation is obtained by replacing the distance to the nearest wall, d, by $\widetilde{d}$, where $\widetilde{d}$ is defined as,

$$\widetilde{d} \equiv \min(d, C_{DES}\Delta)\,. \tag{8}$$

In Eqn. (8) for the current study, Δ is the largest distance between the cell center under consideration and the cell center of the nearest neighbors (i.e., those cells sharing a face with the cell in question). In "natural" applications of DES, the wall-parallel grid spacings (e.g., streamwise and spanwise) are on the order of the boundary layer thickness and the S-A RANS model is retained throughout the boundary layer, i.e., $\widetilde{d} = d$. Consequently, prediction of boundary layer separation is determined in the 'RANS mode' of DES. Away from solid boundaries, the closure is a one-equation model for the SGS eddy viscosity. When the production and destruction terms of the model are balanced, the length scale $\widetilde{d} = C_{DES}\Delta$ in the LES region yields a Smagorinsky eddy viscosity $\widetilde{\nu} \propto S\Delta^2$. Analogous to classical LES, the role of Δ is to allow the energy cascade down to the grid size; roughly, it makes the pseudo-Kolmogorov length scale, based on the eddy viscosity, proportional to the grid spacing. The additional model constant $C_{DES} = 0.65$ was set in homogeneous turbulence (Shur *et al.* 1999) and is used without modification in this work.

2.2 Approach and simulation overview

As measured by Polhamus *et al.* (1959), there are important Reynolds number effects in the flow around the forebody at angle of attack. These effects are analogous to that of the drag crisis occurring around cylinders and spheres and are linked to boundary layer transition and the nature of the flow separation. While predicting details of the transition process is beyond the scope of the methods used in the current simulations, it is possible to construct well-defined computations to investigate the effect of the type of boundary layer separation on the flow. In particular, simulations were performed in the sub- and super-critical regimes in which the type of boundary layer separation was controlled via the initial and boundary conditions on the eddy viscosity.

Following, Travin *et al.* (2001), a 'tripless' approach is employed for sub-critical flows in which the inflow eddy viscosity is zero. Non-zero values are seeded into the wake and the reversed flow that is established in the recirculating region is sufficient to sustain the turbulence model downstream of separation. Boundary layer separation in this case is laminar with the model active following separation. For the super-critical flows the inflow eddy viscosity is set to a small value (3ν), sufficient to ignite the turbulence model on solid surfaces as the fluid enters the boundary layers. The subsequent separation is then of a turbulent boundary layer.

The computations were performed using Cobalt$_{60}$, an unstructured finite-volume method developed for solution of the compressible Navier-Stokes equa-

Table 1. Simulation parameters. Grid size reported as surface-normal × surface-tangential × spanwise; "baseline" is the smaller x–y domain, "padded" the larger x–y domain. URANS calculations performed using the Spalart-Allmaras one-equation model.

Case	Model	Grid Size	L_z	x–y domain
1	DES	$100 \times 149 \times 151$	$3D$	baseline
2	DES	$100 \times 149 \times 301$	$6D$	baseline
3	DES	$150 \times 200 \times 151$	$3D$	baseline
4	DES	$120 \times 149 \times 151$	$3D$	padded
5	DES	unstructured, 3.55×10^6 cells	$3D$	padded
6	MILES	$120 \times 149 \times 151$	$3D$	padded
7	URANS	200×400	–	baseline
8	URANS	$120 \times 149 \times 151$	$3D$	padded

tions and described in Strang *et al.* (1999). The numerical method is a cell-centered finite volume approach applicable to arbitrary cell topologies (e.g, hexahedrals, prisms, tetrahdrons). The spatial operator uses the exact Reimann Solver of Gottlieb and Groth (1988), least squares gradient calculations using QR factorization to provide second order accuracy in space, and TVD flux limiters to limit extremes at cell faces. A point implicit method using analytic first-order inviscid and viscous Jacobians is used for advancement of the discretized system. For time-accurate computations, a Newton sub-iteration scheme is employed, the method is second order accurate in time.

For parallel performance, Cobalt$_{60}$ uses the domain decomposition library ParMETIS (Karypis *et al.* 1997) to provide nearly perfect load balancing with a minimal surface interface between zones. Communication between processors is achieved using Message Passing Interface (MPI), with parallel efficiencies above 95% on as many as 1024 processors (see also Grismer *et al.* 1998).

Most of the calculations presented in the next section were performed on structured meshes. Structured grids were generated using the control technique of Hsu and Lee (1991). Using this technique, it was possible to control mesh spacing to the first point nearest the boundary (within one wall unit near solid surfaces), exert control over grid spacing tangential to the boundary, and also to maintain orthogonality of the mesh at all boundaries. Also evaluated in the next section is a DES prediction obtained on an unstructured mesh. The unstructured grid was generated using Gridgen (Steinbrenner *et al.* 2000), with prisms in the boundary layer and near-isotropic tetrahedra away from solid surfaces. The ability to exert greater control on cell distribution compared to the structured grids permitted generation of an unstructured mesh having 2.5×10^6 cells (of a total cell size of 3.55×10^6 cells) within two diameters of the model surface.

The parameters of the calculation are summarized in Table 1. Shown is the case number, model, grid size, spanwise period, and reference to the x–y domain size. The majority of simulations were performed on domains in which the spanwise dimension was three times the diameter, i.e., $L_z = 3D$. The influence of the spanwise period was investigated in Case 2 via computations performed on a domain with a doubling of the spanwise period to $L_z = 6$. Domain-size influences were also investigated in calculations with two domains having different outer-boundary placement. The smaller domain (referred to as "baseline" in the table) extended eight diameters downstream of the body and with a lateral extent also of $8D$. In calculations performed on the larger domains (referred to as "padded" in the table), the streamwise extent to the outflow boundary downstream of the body was at approximately $20D$, with the lateral dimension also approximately $20D$ from the model surface. As shown in the next section, there was an overly strong effect of the baseline domain on the solutions, resulting in over-predictions of the stagnation pressure and axial force. Boundary conditions on the model surface were no-slip for the velocity components and turbulent viscosity. The normal momentum equation is used at solid walls to estimate the variation of pressure normal to the surface, while a one-sided, least-squares gradient method is used to estimate the variation of pressure tangential to the wall.

Grid resolution effects were investigated by refining the mesh in the x–y plane by a factor of two. For the coarse grid with the shorter spanwise dimension ($L_z = 3D$), the structured-grid calculation was performed using approximately 2.2×10^6 points, the finer mesh calculation possessing about 4.5×10^6 grid points. Because Δ in Eqn. (8) near the surface was set by the spanwise spacing, the thickness of the "RANS region", i.e., the dimension from the model surface to the interface at which $\widetilde{d}$ is set by the grid spacing for all the DES runs was $0.013D$. The dimensionless timestep, $\Delta t/(D/U_\infty)$ (U_∞ is the freestream speed), was 0.01, a conservative value chosen based on preliminary calculations and previous time-accurate computations of unsteady flows by the current investigators and other researchers (e.g., see Travin *et al.* 2001). With $\Delta t/(D/U_\infty) = 0.01$, there are approximately 350 timesteps per main shedding cycle.

From a given set of initial and boundary conditions for a particular flow type (tripless or fully-turbulent), the governing equations were time advanced through a transient as the flow evolved to its equilibrium condition. This transient, typically less than $20D/U_\infty$, was discarded and the simulations continued for an additional period of $\mathcal{O}(100D/U_\infty)$. This period was sufficient for adequate convergence of averaged quantities and capture of the long timescales in the flow.

3. Results

3.1 Solution properties and flow visualization

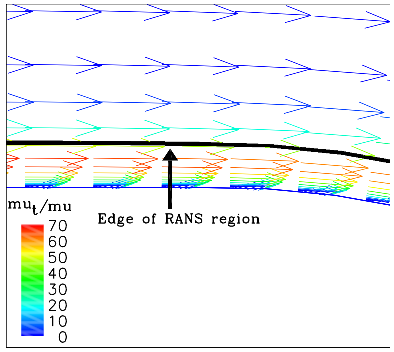

Figure 2. Flow field near upper-rear corner of the forebody. Dark border marks edge of the "RANS region" at $0.013D$. Velocity vectors colored by viscosity ratio ν_t/ν.

A snapshot of the instantaneous velocity vectors in a plane near the upper rear corner (θ in the range $45°$) for a turbulent separation run (simulation parameters correspond to Case 4) is shown in Figure 2. The interface beyond which $\tilde{d}$ is set by the grid has been drawn. The figure shows a smooth transition between the "RANS region" and "LES region" of the solution with essentially all of the boundary layer within the RANS region.

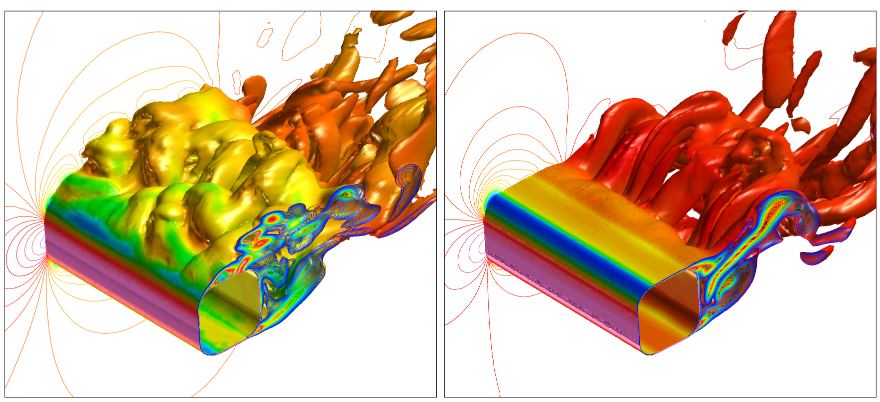

Figure 3. Instantaneous vorticity isosurfaces with pressure contours on the far plane, vorticity contours in the near plane. Sub-critical flow at $Re = 10^5$ shown on the left, super-critical flow at $Re = 8 \times 10^5$ shown on the right.

The different structure of the sub- and super-critical flows is illustrated in Figure 3. Drawn for each flow-type are isosurfaces of the instantaneous vorticity field (colored by the local pressure). Contours of pressure and vorticity are shown on the far and near periodic planes, respectively. For the sub-critical flow at $Re = 10^5$ the attached boundary layers are laminar and cannot sustain the development of the adverse pressure gradient in the upper front corner with separation occurring around $\theta \approx 135°$. In the "tripless" mode, the turbulence model is dormant upstream of separation, with flow reversal sustaining the model downstream of separation.

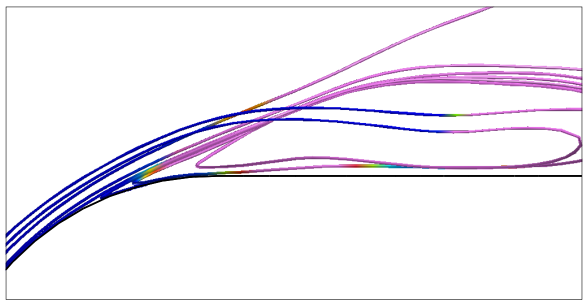

Figure 4. Particle pathlines colored by ν_t/ν from tripless solution at $Re = 10^5$. Threshold of ν_t/ν from 0 (blue) to 1 (purple).

Shown in Figure 4 are a representative sample of pathlines in the vicinity of the upper front corner of the forebody for the flow at $Re = 10^5$ (simulation parameters correspond to Case 4 in Table 1). The pathlines in the figure are colored by the value of the viscosity ratio ν_t/nu. Upstream of separation the eddy viscosity is zero (as indicated by the blue color of the pathline). In the separated region the reversing flow sweeps turbulent fluid from downstream into contact with the separating flow. Important to note is that there is not a "transition creep", i.e., a numerical diffusion of non-zero eddy viscosity into regions upstream of separation.

In "natural" applications of DES, the detached regions of the flow are computed using LES, in this case with a one-equation model for the subgrid-scale eddy viscosity. An advantage of LES is that mesh refinement resolves more flow features, in turn lessening modeling errors and driving the solution towards the DNS limit. The effect of mesh refinement was investigated by doubling the x–y grid by a factor of two in Case 3 as compared to Case 1 (c.f., Table 1). Shown in Figure 5 are instantaneous vorticity contours from Case 1 and Case 3 for a simulation with turbulent boundary layer separation at $Re = 8 \times 10^5$. Cuts of the vorticity field from three spanwise planes are shown for each case and provide an example of the strong spanwise variation in the DES solution. As also the case for classical LES, Figure 5 shows that the effect of the mesh refinement is to resolve smaller-scale eddies in Case 3. This feature in the DES was also illustrated in the circular cylinder calculations of Travin *et al.* (2001).

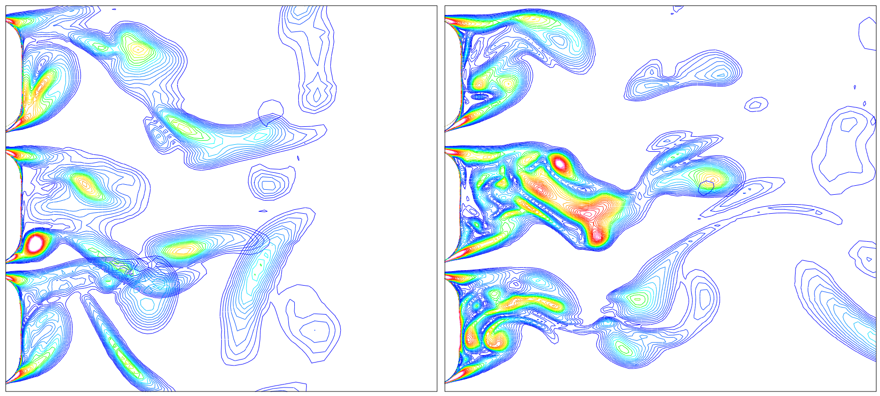

Figure 5. Contours of the instantaneous vorticity in three spanwise planes for Case 1 (on the left) and Case 3 (on the right). Vorticity contours are from a turbulent separation case at $Re = 8 \times 10^5$.

3.2 Statistics for the turbulent separation cases

Force coefficients C_x and C_y in the axial and lateral directions, respectively, are defined using the freestream density and velocity and frontal area of the forebody. Figure 6 shows the force coefficient time histories for the two-dimensional URANS solution at $Re = 8 \times 10^5$. A fraction of the time history is shown in the figure, i.e., following the initial transient. The figure shows the 2D URANS solution is temporally periodic, with large swings in the side force coefficient compared to the axial value as the flow undergoes a shedding cycle.

A representative force coefficient history for a DES run is shown in Figure 7, for a turbulent separation run at $Re = 8 \times 10^5$ (simulation parameters correspond to Case 2). Similar to Figure 6, a transient of roughly 20 non-dimensional time units has been excluded from the figure (note also the longer time integration for the DES). Unlike the 2D URANS, a strong modulation is apparent in the side force coefficient C_y, similar to that observed in related studies of cylinders and other bluff bodies (e.g., see Travin *et al.* 2001). The side-force modulation is complex and seems to be an intrinsic feature of the chaotic, three-dimensional flow. For the forebody, the modulation develops via the interaction of spanwise and streamwise vorticity in the near wake. DES calculations on domains in which the spanwise coordinate L_z was $1.5D$ did not yield force modulation and suppressed three-dimensionality of the primary spanwise structure (although the solution possessed streamwise vorticity). Predictions on the domain with $L_z = 1.5D$ yielded large over-predictions of the

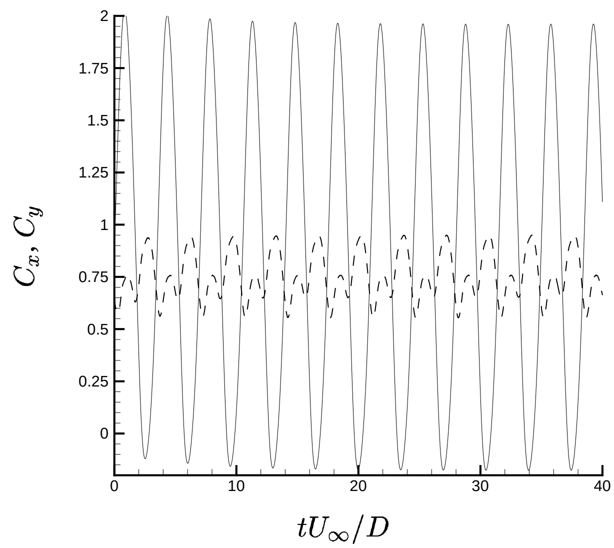

Figure 6. Force coefficients C_x and C_y from two-dimensional URANS at $Re = 8 \times 10^5$, turbulent boundary layer separation. ---- C_x; ——— C_y.

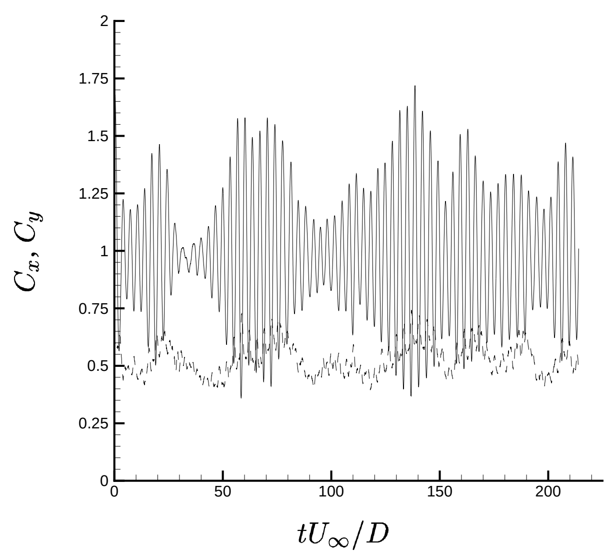

Figure 7. Force coefficients C_x and C_y from Case 2, DES prediction at $Re = 8 \times 10^5$, turbulent boundary layer separation. ---- C_x; ——— C_y.

Table 2. Time-average force coefficients from turbulent separation cases at $Re = 8 \times 10^5$ (time averages denoted using $\langle\cdot\rangle$). Experimental measurements are from Polhamus *et al.* (1959).

Case	Model	$\langle C_x \rangle$	$\langle C_y \rangle$
1	DES	0.57	0.92
2	DES	0.55	0.98
3	DES	0.51	0.96
4	DES	0.46	0.94
5	DES	0.43	0.83
6	MILES	0.76	0.62
7	2D URANS	0.75	0.88
8	3D URANS	0.43	0.94
–	expts.	0.4	0.9

axial force. Though not shown here, force-coefficient histories for all of the three-dimensional turbulent separation cases – including the 3D URANS result – exhibited force modulation.

Time-averaged force coefficients for the turbulent separation cases are summarized in Table 2. The 2D URANS, which produces a periodic shedding and cannot accurately account for the force modulation, substantially over-predicts the mean axial force coefficient $\langle C_x \rangle$. This feature is analogous to the circular cylinder where two-dimensional URANS yields large drag (Travin *et al.* 2001). For the DES, force coefficients from the smaller (baseline) domains are higher than the measured values as well as from calculations performed on the larger domain (c.f., Cases 1-3). A comparison of Case 3 against Cases 1-2 show a trend towards lower axial force with grid refinement in the x–y plane. In addition, the axial force slightly decreases in Case 2, computed on the longer spanwise domain, compared to Case 1. Nevertheless, $\langle C_x \rangle$ is too high and, as shown below, the over-prediction arises from the influence of the computational domain, which effectively constrains the flow and raises the stagnation pressure by about 10% compared to results obtained on the larger domains (Cases 4-5). DES predictions on the larger domain using both structured and unstructured grids are in quite good agreement with the measurements of Polhamus *et al.* (1959). Interestingly, the 3D URANS also yields forces in good agreement with the measurements and padded-domain DES predictions. On the other hand, calculations without an explicit turbulence model (Case 6) markedly over-predict the axial force due to the poor treatment of the attached boundary layers, as described in more detail below.

Pressure coefficients around the body for the fully-turbulent runs ($Re = 8 \times 10^5$) are shown in Figure 8. The angle θ is measured counter-clockwise from the aft-symmetry point of the forebody. For the flow at $10°$ angle of attack, the maximum C_p occurs about $15 - 20°$ below the fore-symmetry point ($\theta \approx$

$-160°$ as shown in Figure 8). For Cases 1, 3, and 7, the stagnation C_p is over-predicted, an error introduced by the use of the smaller x-y domain. For these cases the over-prediction in the stagnation pressure is $\mathcal{O}(10\%)$, comparable to the over-prediction of the mean axial force (c.f., Table 2). Comparing the effect of the domain (Case 1 and Case 4) shows a reduction in the axial force coefficient on the larger domain, closer to the measured value of about 0.4 as also summarized in Table 2. The 2D URANS, with a finer x-y grid compared to the three-dimensional runs also shows deeper minima in C_p in the vicinity of each corner, providing some insight into the effect of grid resolution on the pressure field.

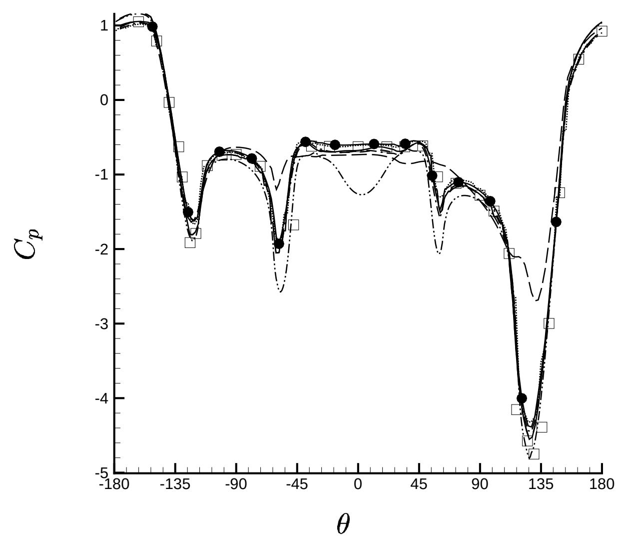

Figure 8. Pressure coefficient distribution around the forebody. Turbulent separation cases, $Re = 8 \times 10^5$. Symbols are measurements from Polhamus *et al.* (1959). ——— Case 1; – – – – Case 3; —·— Case 4; ········ Case 5; — — — — — Case 6; —··— Case 7; ●——● Case 8.

An effect of the Reynolds number reproduced in the fully-turbulent solutions in Figure 8 is that the boundary layers around the upper front and lower front corners ($\theta \approx \pm 135°$) remain attached, as evidenced by the strong pressure minima in these regions, especially around $\theta \approx 135°$. It is apparent that all of the simulations predict attached boundary layers around the upper front corner, with the exception of the MILES run (Case 6), i.e., the simulation performed without an explicit turbulence model in which the (laminar) boundary layer separates. Accurate prediction of boundary layer growth and separation in MILES requires the boundary layer grid be sufficiently fine to resolve the small near-wall turbulent structures (as would also be required in whole-domain LES with an explicit SGS model). In practice, however, boundary layer grids will not be sufficiently dense for high Reynolds numbers flows because of the high computational cost. In the present case, the resulting MILES boundary layer prediction is absent of turbulent structures and is essentially laminar.

Along the rear vertical surface (in the vicinity $\theta = 0$ in Figure 8) the 2D URANS (Case 7) pressure distribution is far from the measured values, resulting in a large streamwise force (c.f., Table 2) as also observed in other two-dimensional URANS predictions of bluff-body flows (e.g., see Travin *et al.* 2001). For all other cases shown in the figure, including the 3D URANS, predictions of the rear-surface pressures are reasonable, close to the measurements of Polhamus *et al.* (1959). Consequently, for the DES and 3D URANS calculations on the padded domains (Cases 4, 5, and 8), the overall pressure distributions are adequate and the axial and streamwise forces exhibit reasonable agreement with measurements. The accuracy of the 3D URANS result is surprising since flow visualizations show the solution lacks the streamwise vorticity apparent in the DES predictions shown in Figure 3. Flow visualizations show that the 3D URANS solution exhibits weak, but persistent, three-dimensionality in the primary spanwise vorticity shed from the forebody. Because the peak suction is missed in the MILES run (Case 6), the axial force is too high, yielding a similar $\langle C_x \rangle$ as the 2D URANS, though the causes for the over-predictions by these two techniques are not the same.

Mean side-force coefficients summarized in Table 2 show that the DES predictions of the lateral force coefficient $\langle C_y \rangle$ are in general not far from the measurements reported by Polhamus *et al.* (1959). The lateral force prediction in the MILES case provides another illustration of the error that can arise due to the boundary layer treatment in this technique. As also noted in the C_p distribution and axial force coefficient, the 3D URANS is again accurate and apparently able to resolve enough of the 3D variation important to accurate prediction.

3.3 Statistics for the laminar separation cases

Laminar separation cases in the DES were computed for most of the simulation parameters summarized in Table 1. The Reynolds number in the laminar separation runs was 1×10^5 for the DES (4×10^5 for the 2D URANS shown below), below the critical value found by Polhamus *et al.* (1959) of approximately 5×10^5. In the tripless mode, the upstream eddy viscosity was zero throughout the simulation. The wake was initially seeded with eddy viscosity and the reversing flow established behind the forebody is sufficient to sustain the turbulence model following separation.

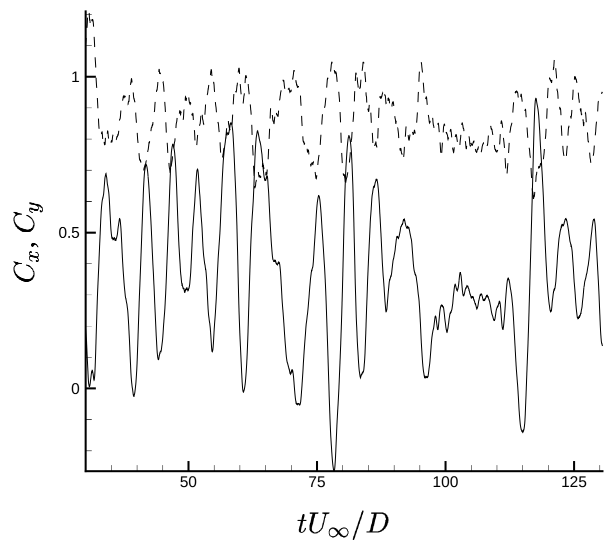

Figure 9. Force coefficients C_x and C_y from Case 4, DES prediction at $Re = 1 \times 10^5$, laminar boundary layer separation. ---- C_x; ——— C_y.

A representative force history from a laminar separation case is shown in Figure 9. The simulation parameters for this case correspond to those of Case 4 in Table 1. As shown qualitatively via Figure 3, below the critical Reynolds number the flow separates in the vicinity of the upper front corner of the forebody. The measurements of Polhamus *et al.* (1959) indicate that the boundary layer along the lower surface of the forebody remains attached. The pressure distribution is then to develop lower pressures along the lower forebody surface compared to the upper surface, which has the result of reversing the magnitude of the side force as compared to the values measured at higher Reynolds numbers, past the critical value.

The force histories shown in Figure 9 show a higher axial force than in the fully turbulent runs discussed above. The mean axial force for this case is around 0.8, not far from the value reported in Table 2 for the MILES run at $Re = 8 \times 10^5$, which also experiences flow detachment in approximately the same region near the upper front corner. More importantly, the side force C_y in Figure 9, while chaotic, is only infrequently negative. Therefore, the mean side force will not be negative (the mean C_y is 0.38 for the trace in Figure 9) and the simulation does not yield a reversal in the magnitude of the side force.

The pressure coefficient distribution around the forebody for the laminar separation DES (Case 4 parameters) is shown along with the experimental measurements of Polhamus *et al.* (1959). For comparison, the C_p distribution

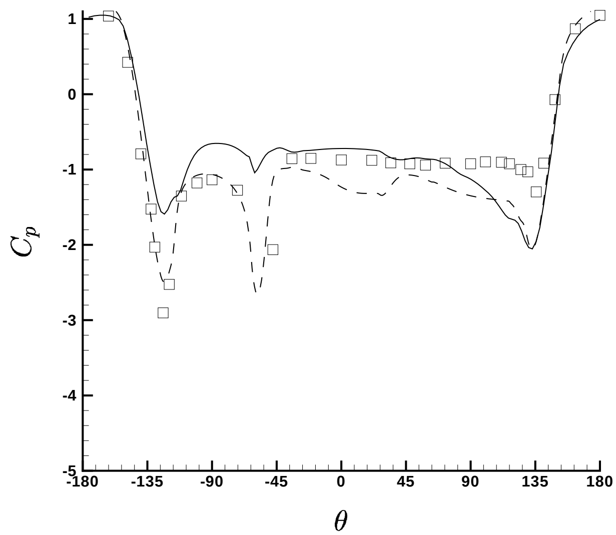

Figure 10. Pressure coefficient distribution around the forebody. Laminar separation cases. Symbols are measurements from Polhamus *et al.* (1959). ——— Case 4 ($Re = 1 \times 10^5$); ---- Case 7 ($Re = 4 \times 10^5$).

from the 2D URANS calculation at $Re = 4 \times 10^5$ is also shown. Consistent with the flow visualization shown in Figure 3, flow detachment around $\theta \approx 135°$ results in a substantially higher C_p compared to the turbulent separation case in Figure 8. Both the DES and 2D URANS have lower minima, indicative of delayed boundary layer separation as compared to the experiments. Near the lower front surface ($\theta \approx -135°$), measurements show a deeper minima than predicted in the DES. The 2D URANS, on the other hand, comes closer to predicting the pressure minima along the lower surface. Along the rear vertical surface ($\theta \approx 0°$), DES predictions of the pressure distribution are reasonable. However, because of the deeper minima in the DES C_p near $\theta \approx 135^o$ and higher C_p along the lower flat surface, side force reversal cannot occur. Inspection of the instantaneous fields shows that along the lower flat surface (in the vicinity of $\theta \approx 135°$), a thin region of reversed flow occurs in the DES (in the mean). This reversed flow region contributes to an effectively altered geometry that prevents development of a deep C_p minimum as apparently occurs in the experiments. To determine if the development of the thin region of reversed flow was caused by numerical and/or modeling errors, a Direct Numerical Simulation of the two-dimensional flow at $Re = 1 \times 10^4$ was conducted using a grid of 1600×1200 points. The DNS result shows a similar thin region of reversed flow along the lower surface of the forebody, near the lower front corner. Though not shown in Figure 10, the C_p distribution for the DNS is similar to the tripless DES prediction at $Re = 1 \times 10^5$.

4. Summary

DES was applied to prediction of the separated flow around a forebody at 10° angle of attack. Influences of domain size, grid refinement, and turbulence model were investigated in flows in which boundary layer separation was either laminar or turbulent. The initial and/or boundary conditions of the calculations set the type of boundary layer separation, corresponding to flows above or below the critical Reynolds number for which there is a reversal of the side force in the experimental measurements of Polhamus *et al.* (1959).

In general, DES predictions of the fully turbulent flow seem robust, tending towards experimental measurements with grid refinement, for example. The complex shedding process and modulation in the forces appear to be represented reasonably adequately, at least in relation to the agreement between simulation and measurement of the pressure distribution and forces. In the sub-critical regime, no simulation technique applied during the course of this study (DES/LES, DNS, and preliminary calculations using vortex methods) yielded a sign change in the side force. Small differences in the geometry, hysteresis, and sidewall effects are three sources that might explain on the differences between predictions of the sub-critical flow and experimental measurements.

Aside from these effects, boundary layer treatment of the sub-critical flow was simplistic. The advantage of the tripless approach is that the simulation parameters are unambiguous. In practice, there can be substantial regions of laminar flow and a prediction of boundary layer transition is required. Details of the separation process and transition to turbulence that inter-mingle continue to strongly challenge current modeling approaches.

In the present application, the attached boundary layers lie entirely within the “RANS region” of the DES solution. As the flow detaches, in the separating shear layers the wake develops new instabilities that results in the rapid growth of a chaotic and three-dimensional wake. The lack of eddy content in the detaching boundary layers represents a relatively small error to the solutions presented here. In other applications, e.g., flows with shallow separations, it will be advantageous and necessary to seed the upstream flow with ‘eddy content’ and LES part of the attached boundary layers prior to separation.

The current study also provided an opportunity to assess the solver and build confidence in the application of a second-order unstructured method for DES applications. The algorithm was sufficiently accurate to capture the growth of instabilities in the wake on both structured and unstructured grids of reasonable density. Streamwise vortices were captured with between five and ten cells in both cases. These features are connected to aspects of the numerical method, such as least-squares calculations of spatial derivatives and the use of non-linear dissipation (i.e., a TVD type limiter). Higher order methods should be expected to retain a given solution quality while reducing the number of cells required. However, obtaining higher order solutions on an unstructured grids is significantly more challenging than on structured grids. Additionally, higher order methods would likely reduce the scalability of the algorithm. A side-by-side comparison to a higher-order numerical method would provide important estimates of potential benefits to going higher order, in turn allowing one to determine the tradeoffs between various approaches. DES predictions on the unstructured grid showed the potential benefit of the unstructured approach in placing points precisely where they are needed – in the near wake. This study, however, is certainly not a comprehensive testing of the numerics, since it only included experimental surface pressures for validation. More detailed comparions, including wake profiles and spectra are needed to further assess the current approach.

Acknowledgments

The authors gratefully acknowledge the support of AFOSR Grant F49620-00-1-0050 (Program Manager: Dr. Tom Beutner). The bulk of the computations were performed at the Maui High Performance Computing Center (HPCC) and NAVO Major Shared Resource Center (MSRC). The support and cpu hours from each of these centers are gratefully acknowledged.

References

Fureby, C. and Grinstein, F.F., “Monotonically integrated large eddy simulation of free shear flows”, *AIAA J.*, **37**, pp. 544-556, 1999.

Gottlieb, J.J. and Groth, C.P.T., “Assessment of Riemann Solvers for Unsteady One-Dimensional Inviscid Flows of Perfect Gases”, *Journal of Computational Physics*, 1988, **78**, pp. 437-458.

Hsu, K. and Lee, S.L., “A Numerical Technique for Two-Dimensional Grid Generation with Grid Control at All of the Boundaries”, *Journal of Computational Physics*, 1991, **11**, pp. 451-469.

Karypis, G., Schloegel, K. and Kumar, V., “ParMETIS: Parallel Graph Partitioning and Sparse Matrix Ordering Library Version 1.0”, University of Minnesota, Department of Computer Science, Minneapolis, MN 55455, July 1997.

Mittal, R. and Moin, P., “Suitability of Upwind-Biased Finite Difference Schemes for Large-Eddy Simulation of Turbulent Flows,” *AIAA J.*, **35(8)**, pp. 1415-1417, 1997.

Polhamus, E.C., Geller, E.W. and Grunwald, K.J., “Pressure and Force Characteristics of Non-circular Cylinders as Affected by Reynolds Number with a Method Included for Determining the Potential Flow about Arbitrary Shapes”, NASA TR R-46, 1959.

Shur, M., Spalart, P. R., Strelets, M., and Travin, A, “Detached-Eddy Simulation of an Airfoil at High Angle of Attack, 4th Int. Symp. Eng. Turb. Modelling and Measurements, Corsica, May 24-26, 1999.

Spalart, P.R. and Allmaras, S.R. “A One-Equation Turbulence Model for Aerodynamic Flows”, *La Recherche Aérospatiale*, 1994, **1**, p. 5.

Spalart, P.R., Jou, W-H., Strelets, M., and Allmaras, S.R., “Comments on the Feasibility of LES for Wings, and on a Hybrid RANS/LES Approach” *Advances in DNS/LES, 1st AFOSR Int. Conf. on DNS/LES*, Aug. 4-8, 1997, Greyden Press, Columbus OH.

Squires, K.D., Forsythe, J.R., Wurtzler, K.E., Strang, W.Z., Tomaro, R.F., Grismer, M.J., and Spalart, P.R., “Towards Prediction of Aircraft Spin”, High Performance Computing User’s Group Conference 2001, Biloxi Miss, June 2001.

Steinbrenner, J., Wyman, N., Chawner, J., “Development and Implementation of Gridgen’s Hyperbolic PDE and Extrusion Methods,” *AIAA 00-0679*, January 2000.

Strang, W.Z., Tomaro, R.F, Grismer, M.J., “The Defining Methods of Cobalt$_{60}$: a Parallel, Implicit, Unstructured Euler/Navier-Stokes Flow Solver,” *AIAA 99-0786*, January 1999.

Tomaro, R.F., Strang, W.Z., and Sankar, L.N., “An Implicit Algorithm for Solving Time Dependent Flows on Unstructured Grids,” *AIAA 97-0333*, January 1997.

Travin, A., Shur, M., Strelets, M. and Spalart, P., “Detached-Eddy Simulations past a Circular Cylinder”, *Flow, Turbulence and Combustion*, 2001.